Supporting Information - Appendix

Nanoscale magnetic resonance imaging

C. L. Degen[1], M. Poggio[1,2], H. J. Mamin[1] , C. T. Rettner[1] and D. Rugar[1]

[1]*IBM Research Division, Almaden Research Center, San Jose, CA 95120, USA.*

[2]*Center for Probing the Nanoscale, Stanford University, Stanford, CA 94305, USA.*

1. MRFM apparatus

The MRFM apparatus is located in a small vacuum chamber ($p<10^{-6}$ mbar) attached to the mixing chamber of a dilution refrigerator and cooled to the operating base temperature of 300 mK. A spring-based isolation system serves to decouple the apparatus from environmental vibrations. The mass-loaded, single-crystal silicon cantilever has an overall length of 120 μm, with a flexible shaft that is 3 μm wide and 100 nm thick (*1*). The silicon mass located at the end of the cantilever is approximately 1.3 μm thick. The motion of the cantilever is detected using a fiber-optic interferometer (25 nW laser power, λ = 1550 nm). The cantilever has resonance frequency f_c = 2.9 kHz, intrinsic quality factor Q = 30,000 and spring constant k = 86 μN/m. Under measurement conditions (*i.e.*, at 2.482 T external field with the cantilever end positioned within 30 nm of the magnetic tip), the *Q*-factor drops to a few thousand. Active damping using feedback further lowers the effective *Q* to about 300 and speeds up the cantilever response time to ~30 ms (*2, 3*). The resulting force noise was in the range of 5 – 10 aN/Hz$^{1/2}$, depending on the specific positioning of the cantilever over the magnetic tip.

The Cu microwire is 2.6 μm long, 1.0 μm wide, and 200 nm thick. It generates an rf field strength $B_{rf} \approx 3$ mT at the center frequency $\omega_0 / 2\pi = 114.8$ MHz when using an rf current of 15 mA. Power dissipation is about 200 μW. The magnetic tip on the microwire is fabricated using electron beam lithography and a lift-off process. The tip material is deposited by electron beam evaporation and consists of the stack 15 nm Ti / 200 nm $Fe_{70}Co_{30}$ / 15 nm Au. The top Au layer serves to inhibit oxidation of the magnetic FeCo layer. Additional details are available in Ref. (*4*).

2. TMV sample preparation

Purified tobacco mosaic virus (TMV) was purchased from ATCC (catalog number PV-135p) at a concentration of 2,000 μg/ml in a 0.01 M phosphate buffered saline (1x PBS, pH 7.2) and then diluted with additional 1x PBS buffer to 400 μg/ml. The mass-loaded end of the cantilever was prepared by first using a focused ion beam (FIB) to create a flat sample platform about 0.8 μm wide and 1.3 μm high (Fig. 1B). The platform was then coated with 10 nm of Si and 30 nm Au by thermal evaporation. The Au film serves as an electrostatic shield to minimize force noise and is found to promote the adhesion of virus particles. Just before depositing the TMV particles, the cantilever is cleaned by UV/ozone (Bioforce Nanosciences ProCleaner) for 20 minutes in order to remove any organic surface contamination. UV/ozone cleaning renders the Au surface temporarily hydrophilic, which facilitates wetting with the aqueous TMV solution and greatly improves virus particle adhesion. We then dip the cantilever tip into a 10 μl droplet of TMV solution for 2 minutes, retract it and allow it to air dry. For dipping we use a mechanical manipulator stage to approach the cantilever tip vertically towards the droplet with the cantilever's shaft oriented normal to the droplet surface. The tip then enters the solution about 10 μm deep, such that only the very end of the cantilever is

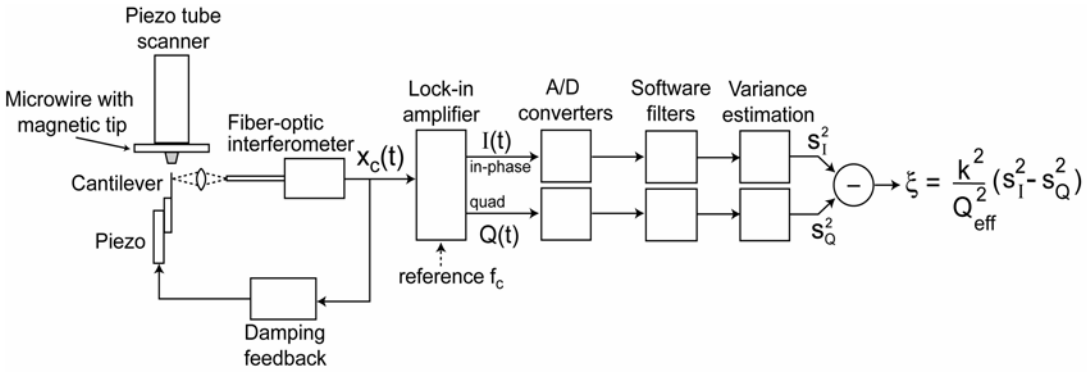

Figure S1 - Key elements for signal detection. Cantilever motion is monitored via a fiber optic interferometer and synchronously detected using a dual-phase lock-in amplifier. The lock-in output is filtered and the spin signal ξ is found by taking the difference of the variances of the in-phase and quadrature waveforms.

exposed to the virus solution. The cantilever with TMV was stored in a dry nitrogen atmosphere for several days before mounting in the MRFM apparatus.

3. Signal generation and detection

Key elements of the MRFM signal detection system are shown schematically in Figure S1. The virus sample is attached to the end of the cantilever, which is positioned close to the magnetic tip. The tip and the integrated microwire are mounted on a piezoelectric tube scanner, which scans the magnetic tip relative to the sample in three dimensions. The cantilever position $x_c(t)$ measured by the interferometer (*5*) is fed into a two-channel lock-in amplifier in order to detect the in-phase and quadrature amplitudes of the cantilever oscillation. The lock-in reference is at the cantilever resonance frequency f_c (approximately 2.9 kHz) and synchronized with the rf frequency modulation that drives cyclic inversions of the protons in the sample. In order to track changes in cantilever frequency during the scan, the cantilever frequency is measured at each scan position while briefly "self-oscillating" the cantilever (*6*).

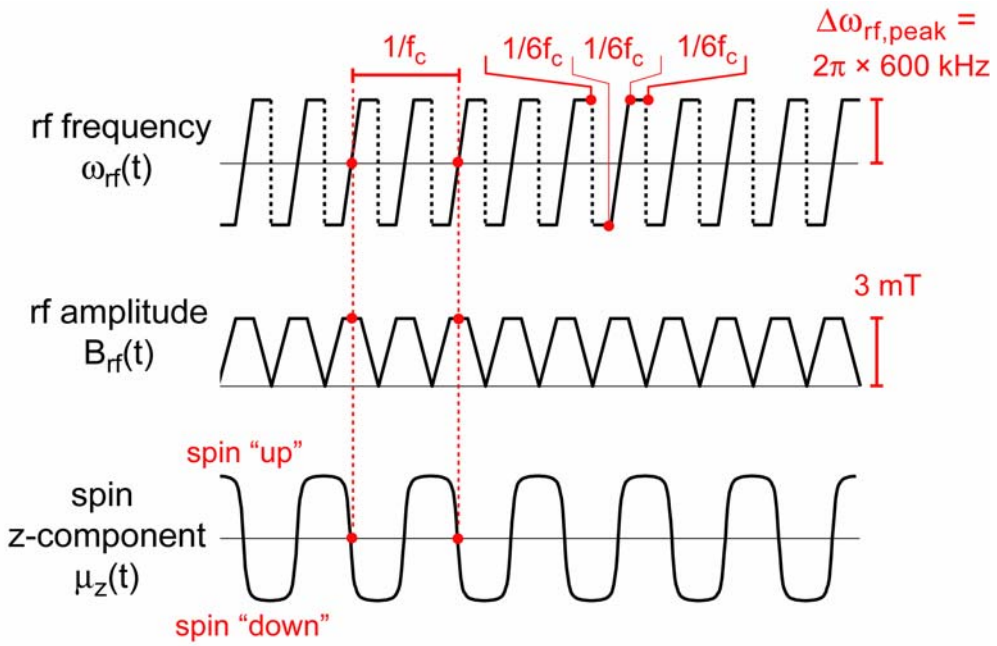

Figure S2 – rf modulation waveforms used to cyclically invert the spins. Cyclic adiabatic inversion is accomplished by sweeping the rf frequency through magnetic resonance twice per cantilever period.

The spins are cyclically inverted using the rf frequency modulation shown in Fig. S2. The rf frequency modulation $\omega_{rf}(t) = \omega_0 + \Delta\omega_{rf}(t)$ consists of unidirectional frequency sweeps (*7*, *8*) with peak deviation $\Delta\omega_{\text{rf, peak}} = 2\pi \times 600$ kHz and repetition rate $2f_c$ (i.e., two spin inversions constitute one full inversion cycle). The sweep duration is 1/6 of a cantilever cycle. A short duration is advantageous since it results in less phase shift in the cyclic inversion for off-resonance spins. The duration cannot be shortened too much, however, without causing problems with adiabaticity. The amplitude of the rf field is strongest during the frequency sweep and ramped to zero at the end of the sweep. This gives more complete inversions for spins that are not centered in the resonant slice and reduces relaxation effects associated with the sudden switching of rf frequency (*8*, *9*). The peak amplitude $B_{rf} \approx 3$ mT is large enough to satisfy the adiabatic condition, $\gamma^2 B_{rf}^2 >> \mathrm{d}\omega_{rf}/\mathrm{d}t$, so that the correlation time of the spins during the

manipulation ($\tau_m \approx 20$ ms) is set by intrinsic spin relaxation effects, and not by the details of the rf protocol, at least for the spins centered in the resonant slice.

The cyclic spin inversions generate an oscillatory attonewton force that excites the cantilever at the mechanical resonance frequency. Typical signal vibration amplitude is a fraction of an angstrom, which is somewhat smaller than the rms amplitude of cantilever thermal vibrations. The lock-in amplifier phase is set so that the spin signal appears predominantly in the in-phase channel for on-resonance spins.

Since the signal originates from the statistical (random) polarization of the spins, the sign of the detected signal can be either positive or negative and fluctuates during the course of the measurement, making conventional signal averaging ineffective. Instead, as discussed in Ref. (*7*), the spin signal is detected via its variance. To estimate the spin signal variance and to distinguish the spin signal from cantilever thermal vibrations, both the in-phase channel $I(t)$ and the quadrature channel $Q(t)$ of the lock-in amplifier are digitized. These signals are then digitally filtered in software using second-order Butterworth filters ($\tau_c = 10$ ms), and the variances s_I^2 and s_Q^2 are calculated.

The cantilever thermal noise contributes equally to s_I^2 and s_Q^2, while the spin signal predominantly adds to s_I^2. The spin signal variance is thus estimated by the difference between the in-phase and quadrature variances (*7*)

$$\xi = \frac{k^2}{Q_{\text{eff}}^2}\left(s_I^2 - s_Q^2\right), \tag{S1}$$

where the factor k^2 / Q_{eff}^2 puts the spin signal variance into units of force squared (e.g., aN^2). We refer to this detected quantity as the "spin variance signal", or simply the "spin signal".

4. Point spread function

Knowledge of the point spread function (PSF), denoted by $K(\mathbf{r})$, is key to understanding MRFM imaging behaviour and central to successful image reconstruction. $K(\mathbf{r})$ is defined as the mean MRFM signal generated by a randomly polarized spin in the sample at a position $\mathbf{r}$ with respect to the magnetic tip. The signal strength is determined by two main factors: 1) the tip field gradient $G \equiv \partial B_z / \partial x$ at the position of the spin, and 2) the effectiveness of the cyclic spin inversions for driving the cantilever vibration. The effectiveness of the spin inversions depends strongly on the position of the spin with respect to resonant slice since spins that are off resonance will not undergo full inversions and the inversion process may be less coherent.

Although a rigorous theory for the point spread function is beyond the scope of this paper, reasonable estimates can be made using some simple models. The key is to understand the off-resonance behaviour of the spin modulation. We start by considering the ideal case where a spin is cyclically inverted by following the effective field in the rotating frame. We then examine a somewhat more sophisticated model based on a numerical simulation of a cantilever coupled to a spin where the spin dynamics are governed by the Bloch equations.

A. Effective field model

The simplest model for adiabatic inversion assumes that the spin follows the effective field in the "rotating frame" – i.e., the reference frame that rotates synchronously with the rf field (*10, 11*). In our case, the effective field is position dependent and can be written as

$$\mathbf{B}_{\text{eff}}(t,\mathbf{r}) = B_{rf}(t)\hat{\mathbf{x}} + \left[\Delta B_0(\mathbf{r}) - \Delta\omega_{rf}(t)/\gamma\right]\hat{\mathbf{z}}, \qquad \text{(S2)}$$

where $B_{rf}(t)$ is the rotating frame rf field amplitude, $\Delta B_0(\mathbf{r}) = B_0(\mathbf{r}) - \omega_0/\gamma$ is the resonance offset, and $B_0(\mathbf{r})$ is the total static field (tip field plus external field). During the frequency modulation, $\mathbf{B}_{\text{eff}}$ changes its orientation with time, and the spin will follow this orientation if the angular rate of change satisfies the adiabatic condition

$$\left|\mathrm{d}\alpha/\mathrm{d}t\right| << \left|\gamma \mathbf{B}_{\text{eff}}\right| \tag{S3}$$

where

$$\alpha(t,\mathbf{r}) = \arctan\left[\frac{B_{rf}(t)}{\Delta B_0(\mathbf{r}) - \Delta\omega_{rf}(t)/\gamma}\right] \tag{S4}$$

Assuming that the spin and effective field are initially aligned or anti-aligned, the z component of the spin magnetic moment during the frequency modulation can then be written as

$$\mu_z(t,\mathbf{r}) = \pm\mu \frac{\Delta B_0(\mathbf{r}) - \Delta\omega_{rf}(t)/\gamma}{\left[\left(B_{rf}(t)\right)^2 + \left(\Delta B_0(\mathbf{r}) - \Delta\omega_{rf}(t)/\gamma\right)^2\right]^{1/2}} \tag{S5}$$

where μ is the proton magnetic moment. The plus sign signifies alignment between the spin and the effective field ("spin locked" case), while the minus sign signifies anti-alignment ("spin anti-locked").

Figure S3A shows waveforms of $\mu_z(t)$ for various values of the off-resonance condition ΔB_0, assuming that the frequency and amplitude modulation are that shown in Fig. S2. We assume a peak frequency deviation of 600 kHz ($\Delta B_{peak} \equiv \Delta\omega_{rf,peak}/\gamma = 14$ mT) and an rf amplitude modulation that ranges from zero to a maximum strength of 3 mT. For the on-resonance case ($\Delta B_0 = 0$), the spin undergoes very complete inversions and alternates between the spin locked and anti-locked states. As the off-resonance condition increases, the waveform shifts in time and

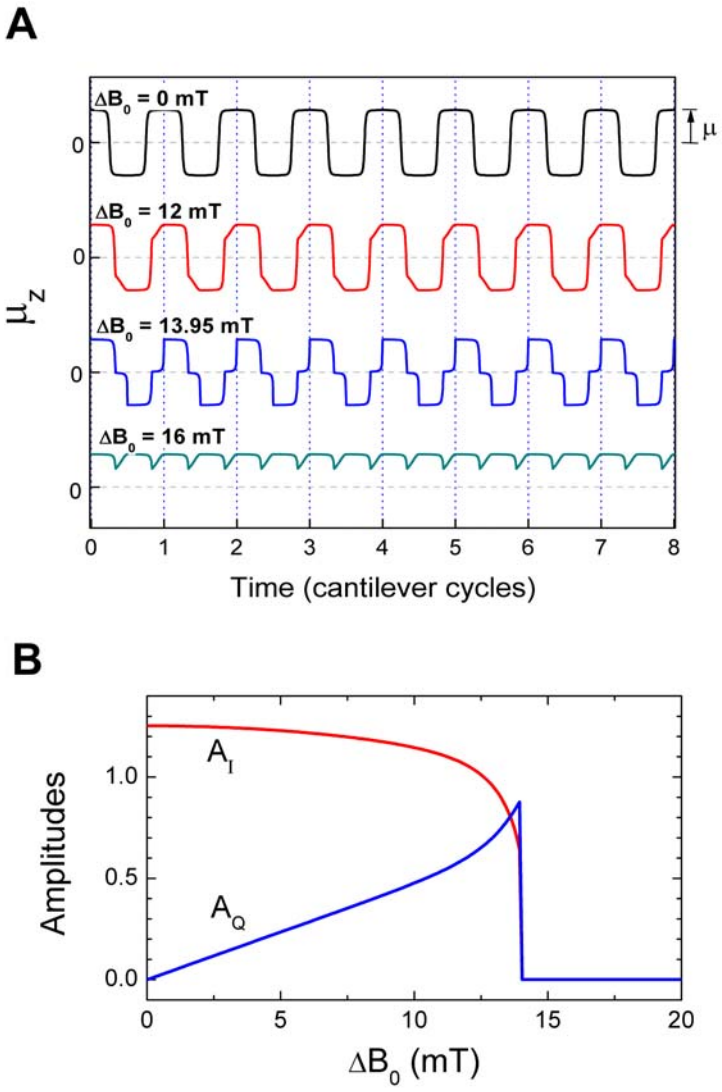

Figure S3 – Results from effective field model. (**A**) Waveforms showing z component of magnetic moment calculated using equation (S5) for various off-resonance conditions ΔB_0 . (**B**) Fourier amplitudes of in-phase (A_I) and quadrature (A_Q) components

becomes distorted. Finally, when $\Delta B_0 > \Delta B_{peak}$, the spin no longer passes through resonance and the inversion ceases.

Waveforms of the type shown in Fig. S3A have been Fourier analyzed to determine their effectiveness for driving a cantilever response. We write $\mu_z(t)$ in terms of the fundamental frequency components as $\mu_z(t) = A_I \mu \cos(\omega_c t) + A_Q \mu \sin(\omega_c t)$ and plot A_I and A_Q as a function of the off resonance condition in Fig. S3B. For small ΔB_0, A_I is of order unity and A_Q is small. As ΔB_0 approaches ΔB_{peak}, A_I diminishes, while A_Q grows. Finally, when $\Delta B_0 > \Delta B_{peak}$, both A_I and A_Q abruptly drop to zero.

The above result is for ideal classical spin behavior. In reality, the spin will undergo random spin flips between the spin-locked and anti-locked states, resulting in random polarities of A_I and A_Q. It is this randomness that necessitates the variance-based signal detection defined by equation (S1). Since the in-phase force is given by $\mu G A_I$, the variance of the in-phase force for a spin with fluctuating orientation will be proportional to $\mu^2 G^2 A_I^2$, and likewise for the quadrature force. Using the definition of the MRFM signal in (S1), which is based on the difference between the in-phase and quadrature variances, we find that the point spread function can be written as

$$K(\mathbf{r}) = A\mu^2 \left[G(\mathbf{r}) \right]^2 \eta\left(\Delta B_0(\mathbf{r}) \right), \tag{S6}$$

where

$$\eta(\Delta B_0) = \frac{A_I^2(\Delta B_0) - A_Q^2(\Delta B_0)}{A_I^2(0)} \tag{S7}$$

is a function characterizing the off-resonance response (normalized so that $\eta(0) = 1$). A is an overall constant, typically close to unity, that depends on the correlation time of

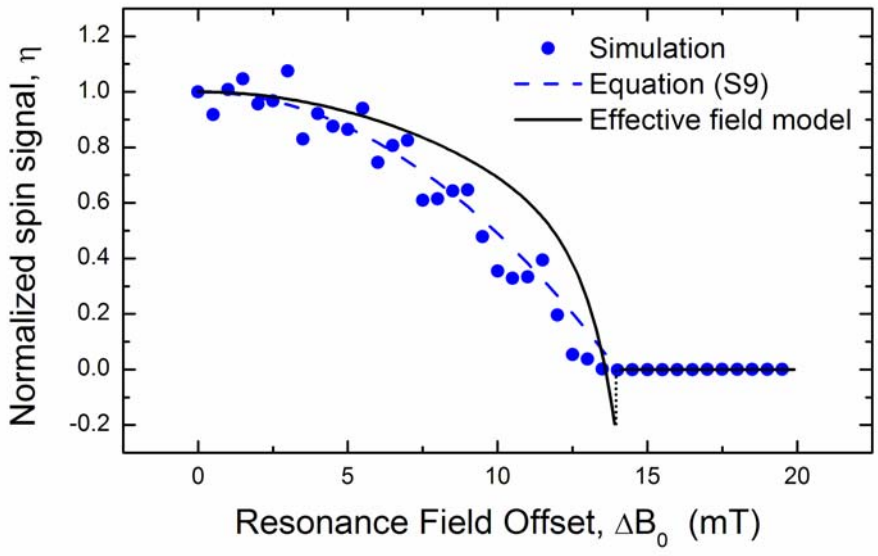

Figure S4 – Normalized spin signal as a function of resonance offset. Solid black line is based on effective field model (S5). Data points are simulation results based on the equations in (S8). The dashed line is the second-order approximation in (S9).

the statistical spin polarization, the lock-in detection bandwidth and the Fourier coefficient of the on-resonance waveform, $A_1(0)$.

A plot of $\eta(\Delta B_0)$ is shown in Fig. S4. As expected, $\eta(\Delta B_0)$ drops as ΔB_0 increases, and eventually attains negative values due to the phase shift of the cyclic inversion waveform. One aspect of the model is clearly unphysical: the discontinuous jump to zero at $\Delta B_0 = \Delta B_{peak}$. Another deficiency of this model is the assumption that the spin follows the effective field even as B_{rf} diminishes to zero due to the amplitude modulation of the rf field. One would expect the spin-lock assumption to break down for small rf field strength. To address these issues, we developed a second model for a cantilever coupled to the spin, where the spin dynamics is governed by the Bloch equations.

B. Simulation based on the Bloch equations

We treat the cantilever as a simple harmonic oscillator coupled to the z component of the spin via the gradient G. The spin dynamics are assumed to be governed by the Bloch equations without relaxation. The coupled equations are:

$$\begin{aligned}
\dot{\mu}_x &= \gamma \mu_y \left[G x_c + \Delta B_0 - \Delta\omega_{rf}(t)/\gamma \right] \\
\dot{\mu}_y &= \gamma \mu_z B_{rf}(t) - \gamma \mu_x \left[G x_c + \Delta B_0 - \Delta\omega_{rf}(t)/\gamma \right] \\
\dot{\mu}_z &= -\gamma \mu_y B_{rf}(t) \\
\ddot{x}_c &+ \frac{\omega_c}{Q_{eff}} \dot{x}_c + \omega_c^2 x_c = G\mu_z / m_c
\end{aligned} \tag{S8}$$

The rf field is assumed to be oriented in the x direction in the rotating frame with amplitude and frequency modulation specified by $B_{rf}(t)$ and $\Delta\omega_{rf}(t)$, respectively. The parameter $m_c = k/\omega_c^2$ is the effective mass of the cantilever and the term $\left[G x_c + \Delta B_0 - \Delta\omega_{rf}(t)/\gamma \right]$ represents the z component of the effective field, including the effect of the cantilever position, the off resonance condition and the rf frequency modulation. These equations were solved step-wise in time using the Runge-Kutta method in order to simulate the behaviour of a randomly oriented spin.

Since the above equations represent the dynamics of an ideal, isolated spin, one additional *ad hoc* assumption was made in the simulation in order to take into account the loss of spin lock for small rf field values. It was assumed that the phase of the spin (i.e., the orientation of the spin in the x-y plane) is randomized when B_{rf} falls below a minimum value, $B_{rf,\min}$. The most appropriate choice for $B_{rf,\min}$ is not obvious. We chose $B_{rf,\min} = 0.5$ mT since we know experimentally that the spin-lock is quite ineffective with such low rf field for protons in organic materials, presumably due to the effect of dipolar interactions. The overall effect of the phase randomization is minimal for spins that undergo full inversions (i.e., for spins that are pointed along the z axis as

B_{rf} goes to zero). However, for spins not fully inverted as the B_{rf} goes to zero, the effect is significant and leads to additional randomization of the spin orientation.

Figure S5 shows a typical simulation result where the cantilever position is plotted as a function of time. The cantilever vibration amplitude is seen to fluctuate with a characteristic correlation time on the order of 30 ms, similar to that observed experimentally. To determine the spin signal from this time record, the cantilever waveform was subjected to a software signal detector equivalent to the hardware version depicted in Fig. S1. Since the spin signal is statistical in nature, the simulation was run 100 times with random initial spin orientations in order to determine the mean signal. Each simulation calculated a 0.5 s time record. This process was repeated as a function of the off-resonance condition ΔB_0 to obtain the normalized response function $\eta(\Delta B_0)$ shown by the points in Fig. S4.

As evident in Fig. S4, both the spin simulation and the effective field model predict that $\eta(\Delta B_0)$ is maximum for $\Delta B_0 = 0$ and falls to zero when $\Delta B_0 > \Delta B_{peak}$. The simulation eliminates the unphysical discontinuity evident in the effective field model. A simple analytical expression is found to fit the simulation data very well:

$$\begin{aligned} \eta(\Delta B_0) &= \left(1 - \frac{\Delta B_0^2}{\Delta B_{peak}^2}\right) \quad \text{for } |\Delta B_0| < \Delta B_{peak} \\ &= 0 \qquad\qquad\quad \text{for } |\Delta B_0| \geq \Delta B_{peak} \end{aligned} \tag{S9}$$

We incorporate this approximation into the expression for the point spread function, yielding

$$\begin{aligned} K(\mathbf{r}) &= A\mu^2 \left[G(\mathbf{r})\right]^2 \left(1 - \frac{\left[\Delta B_0(\mathbf{r})\right]^2}{\Delta B_{peak}^2}\right) \quad \text{for } |\Delta B_0| < \Delta B_{peak} \\ &= 0 \qquad\qquad\qquad\qquad\qquad\quad \text{otherwise} \end{aligned} \tag{S10}$$

This equation is the basis of the PSF shown in Fig. 2 of the main text.

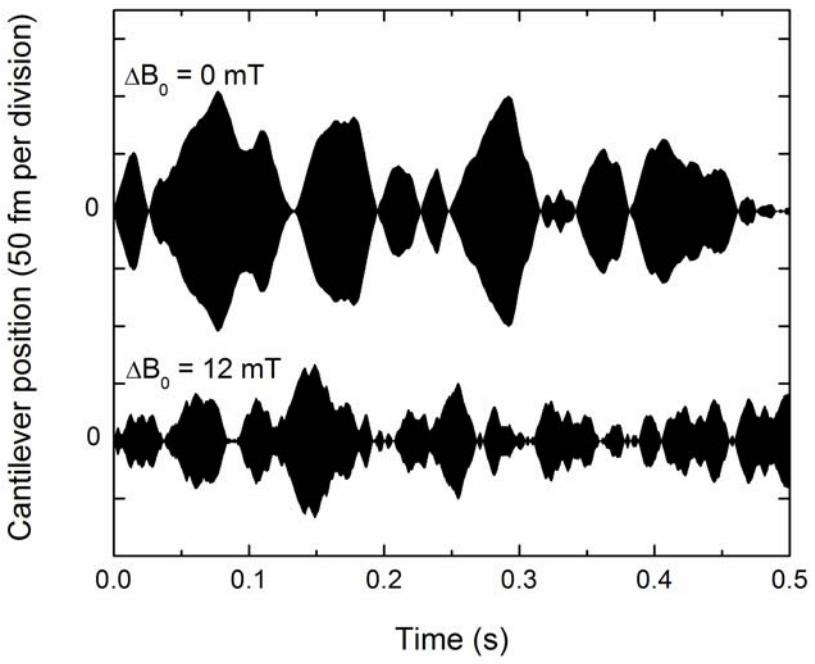

Figure S5 – Typical simulations of cantilever vibration resulting from a proton spin manipulated by the rf frequency and amplitude modulation shown in Fig. S2. The off-resonance signal is significantly smaller and has shorter correlation time. The simulation parameters closely matched those of the experiment: Q_{eff} = 300, $k = 86\ \mu$N/m , $f_c = 2.9$ kHz, $G = 3$ MT/m, $B_{rf} = 3$ mT and $B_{rf,\min} = 0.5$ mT .

5. Magnetic tip model

The point spread function (S10) requires knowledge of the tip field and the tip field gradient. We model the tip as a uniformly magnetized truncated cone with apex radius r_a, base radius r_b and height h. The tip is assumed to be magnetized along the cone axis in the *z* direction with saturation magnetization M_s. On top of the truncated cone, we assume there is a non-magnetic surface layer of thickness *s*, which accounts for the protective overcoat (15 nm of gold) plus a possible additional non-magnetic "dead" layer. The magnetic field from the tip can be calculated by using standard techniques, such as integrating the field from the equivalent surface currents (*12*).

The tip is assumed to be centered about the *z* axis with the topmost (non-magnetic) layer extending up to the plane $z = 0$. The magnetic portion of the tip extends from the base located at $z = -h - s$ to the apex located at $z = -s$. With this geometry, the radial and longitudinal field components are then given by

$$B_r(r,z) = \frac{\mu_0 M_s}{2\pi} \int_{-h-s}^{-s} \frac{z - z'}{r\left[\left(R(z')+r\right)^2 + \left(z-z'\right)^2\right]^{1/2}} \left[\frac{R^2(z') + r^2 + \left(z-z'\right)^2}{\left(R(z')-r\right)^2 + \left(z-z'\right)^2} E(q) - K(q)\right] \mathrm{d}z' \quad \text{(S11)}$$

and

$$B_z(r,z) = \frac{\mu_0 M_s}{2\pi} \int_{-h-s}^{-s} \frac{1}{\left[\left(R(z')+r\right)^2 + \left(z-z'\right)^2\right]^{1/2}} \left[\frac{R^2(z') - r^2 - \left(z-z'\right)^2}{\left(R(z')-r\right)^2 + \left(z-z'\right)^2} E(q) + K(q)\right] \mathrm{d}z' \quad \text{(S12)}$$

Here $R(z') = \frac{r_a - r_b}{h}(z' + s) + r_a$ defines the cone radius for z' from $-h-s$ to $-s$. $E(q)$ and $K(q)$ are the complete elliptic integrals of the first and second kind:

$$K(q) = \int_0^{\pi/2} \frac{\mathrm{d}\theta}{\sqrt{1 - q^2 \sin^2\theta}} \tag{S13}$$

$$E(q) = \int_0^{\pi/2} \sqrt{1 - q^2 \sin^2\theta}\, \mathrm{d}\theta \tag{S14}$$

where

$$q^2 = \frac{4R(z')r}{\left(R(z') + r\right)^2 + \left(z - z'\right)^2}. \tag{S15}$$

The integrals in (S11) and (S12) are easily calculated numerically in order to determine $\mathbf{B}_{\mathrm{tip}}(\mathbf{r})$. The tip field gradient $G = \partial B_z / \partial x$ can also be expressed as a one-dimensional integral that is easily calculated. The expression is a bit too unwieldy to include here, however.

Table S1 shows parameters used for the tip model. To determine these parameters, we first started with the expected saturation magnetization of $Fe_{70}Co_{30}$ ($\mu_0 M_s = 2.4$ T) and with the tip geometry known either from the fabrication process or observed by scanning electron microscopy ($r_a = 100$ nm, $r_b = 175$ nm, $h = 200$ nm and $s = 15$ nm). The field and field gradient were calculated and then used with equation (S10) to determine the point spread function $K(\mathbf{r})$. The tip parameters were then refined by noting key features of the experimental data, such as the distance between the double images in Fig. 3, and comparing them with imaging behaviour expected from the point spread function. In addition, we made a separate set of quantitative measurements of the tip field as a function of spacing by measuring the onset of the MRFM signal at various external fields and tip-sample spacings, as in Ref. (*13*).

The resulting optimized tip parameters are shown in Table S1. One significant difference between the optimized parameters and the initial parameters is that the

Table S1 - Optimized parameters of the magnetic tip

Geometry	Truncated cone magnetized along $\hat{\mathbf{z}}$
Apex radius, r_a	100 nm
Base radius, r_b	160 nm
Height, h	180 nm
Non-magnetic surface layer thickness, s	26 nm
Saturation magnetization, $\mu_0 M_s$	1.51 T
Tilt of sample platform away from tip axis	0° about $\hat{\mathbf{x}}$, -1.7° about $\hat{\mathbf{y}}$
Max. lateral gradient at 24 nm physical spacing. (50 nm magnetic spacing.)	$\left\|\partial B_z / \partial x\right\|_{\max} = 4.2 \times 10^6$ T/m
Max. vertical gradient at 24 nm physical spacing. (50 nm magnetic spacing.)	$\left\|\partial B_z / \partial z\right\|_{\max} = 5.1 \times 10^6$ T/m

saturation magnetization of the tip material is smaller than expected by about 37%. In addition, the non-magnetic surface layer appears to be about 26 nm thick, significantly larger than expected based on the 15 nm thickness of the protective Au overcoat. The reason for these discrepancies is still under investigation. It is likely that these results are at least partially due to oxidation or contamination of the FeCo alloy.

If the tip were operating without these discrepancies, the achievable gradient would be increased by a factor of two. This increase would halve the thickness of the resonant slice and give a proportionate boost to the MRFM imaging resolution. A doubling of the gradient would also quadruple the signal power per spin, which could be used to decrease the measurement time by a factor of 16 at the current spatial resolution, assuming all other factors were equal.

6. Image reconstruction using the Landweber algorithm

Image reconstruction was done numerically using our own Fortran/Labview code following the algorithm outlined by equations (3) and (4) in the main text. The scan data $\xi(\mathbf{r}_s)$ is described by a three-dimensional array where the corresponding grid spacing was 8.3 nm × 16.6 nm × 12.8 nm in $x \times y \times z$. The spin density $\rho(\mathbf{r})$ and point spread function $K(\mathbf{r})$ are described by three dimensional arrays that have grid spacing that is finer than the scan data by factors of 3, 2 and 3 in *x*, *y* and *z*, respectively. In other words, the grid spacing of the arrays for the reconstructed spin density and point spread function corresponds to 2.8 nm × 8.3 nm × 4.3 nm in $x \times y \times z$. Considerable freedom is allowed with regard to the weighting function $\alpha(\mathbf{r})$. Reasonable results are obtained by simply setting $\alpha(\mathbf{r})$ to a constant value. Some improvement was found by allowing $\alpha(z)$ to increase monotonically with *z* up to a prescribed maximum value. The Landweber iterations continued until the error between experimental scan data and the predicted scan data was reduced below 20 aN^2-rms (*i.e.*, below the experimental noise level). The number of iterations to achieve satisfactory convergence was typically a few thousand, depending on the choice for $\alpha(\mathbf{r})$.

Figures S6A and S7A show the raw experimental scan data $\xi(\mathbf{r}_s)$ for the two imaging experiments presented in Figs. 3 and 4, respectively. The figures also show the calculated scan data based on the reconstructed spin density $\rho_n(\mathbf{r}')$. As explained in the main text, the calculated scan data $\xi_n(\mathbf{r}_s)$ is found by computing the convolution integral

$$\xi_n(\mathbf{r}_s) = \int_{\substack{\text{sample}\\ \text{volume}}} \mathrm{d}^3\mathbf{r}'\, K(\mathbf{r}_s - \mathbf{r}')\rho_n(\mathbf{r}'). \qquad \text{(S16)}$$

It is evident that the reconstructions are very effective in producing calculated scan data that is in excellent agreement with the measured scan data. In both cases, the difference between experimental and calculated scan data is less than 20 aN^2-rms, which is comparable to the noise level of the experimental data. This error can be further minimized by continuing the iterations of the Landweber reconstruction, but this is at the expense of adding noise to the reconstructed object.

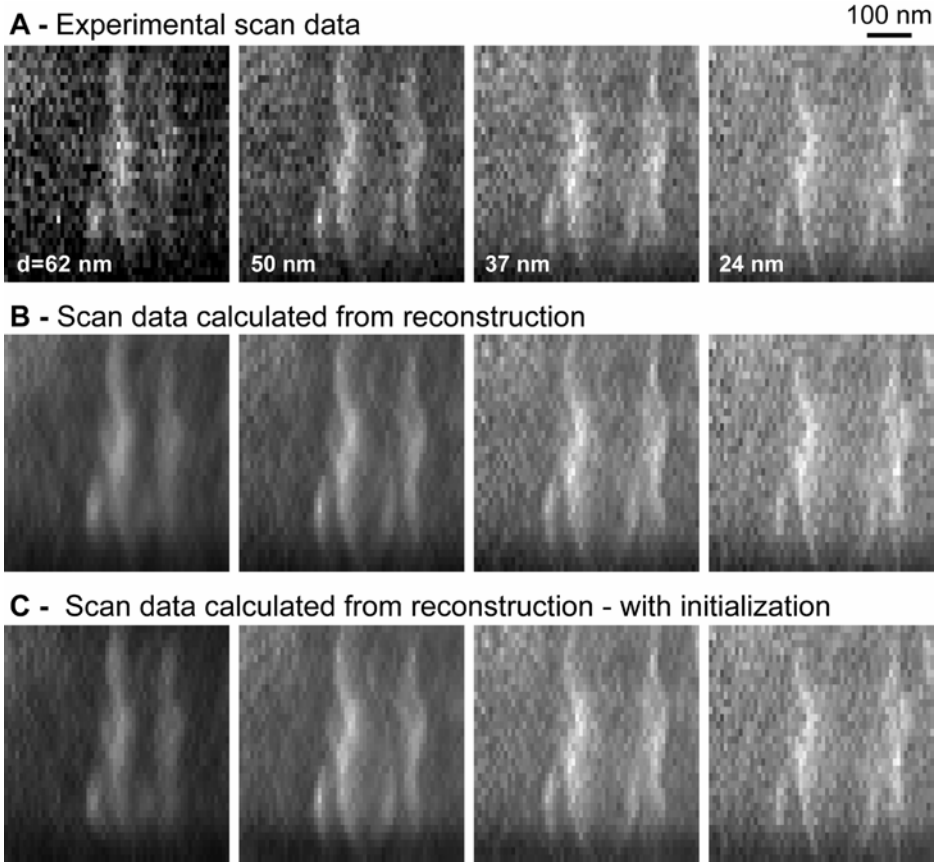

Figure S6 – Comparison of experimental scan data to the data predicted by the reconstruction. (**A**) Experimental data corresponding to Fig. 3 in the main text. Labels indicate the distances between magnetic tip and the virus particles. (**B**) Data predicted from the reconstructed spin density where initial guess in the Landweber reconstruction was zero spin density. (**C)** Same as (**B**), but with the reconstruction initialized assuming a uniform layer of proton spins on the surface.

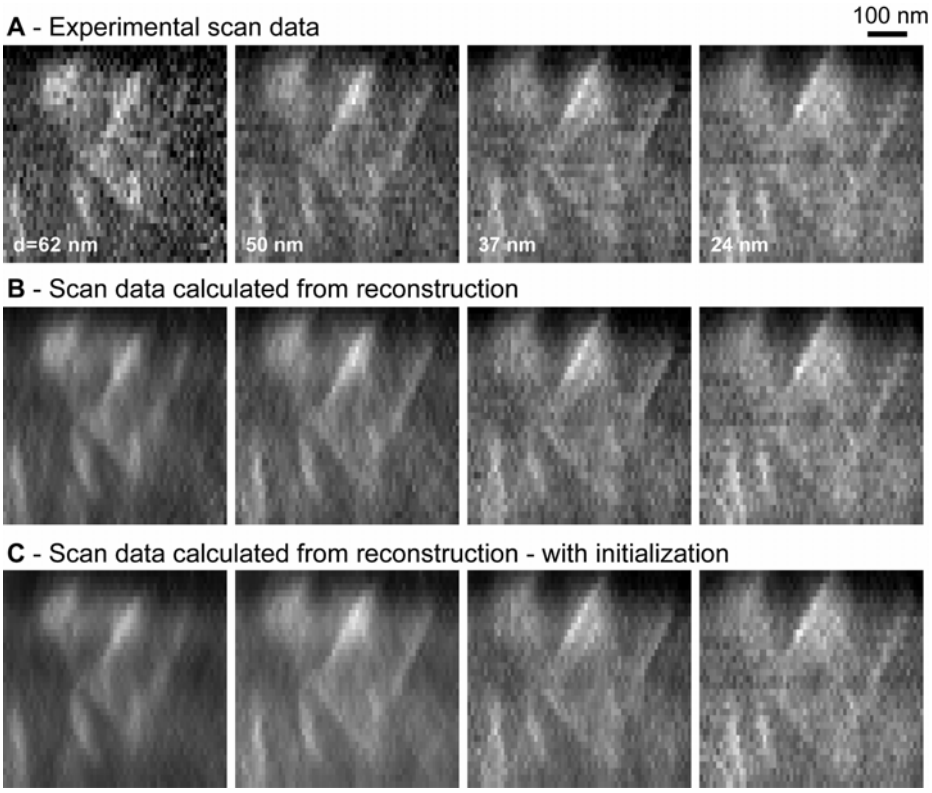

Figure S7 – Comparison of experimental scan data to the data predicted by the reconstruction. (**A**) Experimental data corresponding to Fig. 4 in the main text. Labels indicate the distances between magnetic tip and the virus particles. (**B**) Data predicted from the reconstructed spin density where initial guess in the Landweber reconstruction was zero spin density. (**C)** Same as (**B**), but with the reconstruction initialized assuming a uniform layer of proton spins on the surface.

References

1. Chui BW, Hishinuma Y, Budakian R, Mamin HJ, Kenny TW, Rugar D (2003) Mass-loaded cantilevers with suppressed higher-order modes for magnetic resonance force microscopy. *12th International Conference on Solid-State Sensors and Actuators (Transducers'03)* (IEEE, Piscataway), pp. 1120-1123.
2. Poggio M, Degen CL, Mamin HJ, Rugar D (2007) Feedback cooling of a cantilever's fundamental mode below 5mK. *Phys. Rev. Lett.* 99:017201.
3. Bruland KJ, Garbini JL, Dougherty WM, Sidles JA (1998) Optimal control of ultrasoft cantilevers for force microscopy. *J. Appl. Phys.* 83:3972-3977.
4. Poggio M, Rettner CT, Degen CL, Mamin HJ, Rugar D (2007) Nuclear magnetic resonance microscopy with a microwire rf source. *Appl. Phys. Lett.* 90:263111.
5. Rugar D, Mamin HJ, Geuthner P (1989) Improved fiber-optic interferometer for atomic force microscopy. *Appl. Phys. Lett.* 55:2588-2590.
6. Albrecht TR, Grutter P, Horne D, Rugar D (1991) Frequency-Modulation Detection Using High-Q Cantilevers for Enhanced Force Microscope Sensitivity. *J. Appl. Phys.* 69:668-673.
7. Degen CL, Poggio M, Mamin HJ, Rugar D (2007) Role of Spin Noise in the Detection of Nanoscale Ensembles of Nuclear Spins. *Phys. Rev. Lett.* 99:250601.
8. Madsen LA, Leskowitz GM, Weitekamp DP (2004) Observation of force-detected nuclear magnetic resonance in a homogeneous field. *Proc. Nat. Acad. Sci.* 101:12804-12808.

9. Degen CL (2005) Magnetic resonance force microscopy: NMR spectroscopy on the micro- and nanoscale. PhD thesis (ETH, Zurich).

10. Slichter CP (1996) *Principles of Magnetic Resonance* (Springer, Heidelberg), pp. 23-24.

11. Garwood M, DelaBarre L (2001) The return of the frequency sweep: designing adiabatic pulses for contemporary NMR. *J. Magn. Res.* 153:155-177.

12. Craik D (1997) *Magnetism - principles and applications* (Wiley, New York), pp. 334-336.

13. Mamin HJ, Poggio M, Degen CL, Rugar D (2007) Nuclear magnetic resonance imaging with 90-nm resolution. *Nature Nanotechn.* 2:301-306.